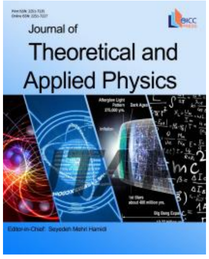

Volume 19, Issue 6, 192558 (1-13)

Journal of Theoretical and Applied Physics
(JTAP)

https://doi.org/10.57647/j.jtap.2025.1906.58

Theoretical Analysis of Coupling Channels in Fusion and Elastic Scattering Reactions for ^{12}C +^{208}Pb, ^{16}O+^{64}Zn and ^{16}O+^{208}Pb Systems

Fatima M. Hussain[1], Mohanad H. Meteab[2], Fouad A. Majeed[1,*]

[1]*Department of Physics, College of Education for Pure Sciences, University of Babylon, Babylon, 51002, Iraq*

[2]*General Directorate of Education in Babylon Governorate, Ministry of Education, Baghdad, 51001, Iraq*

***Corresponding author:** fmajeed@uobabylon.edu.iq

Original Research

Received:
15 April 2025

Revised:
29 May 2025

Accepted:
19 October 2025

Publish online:
31 December 2025

Abstract

In the present study, the reactions of fusion and elastic scattering of the stable, tightly restricted projectiles in ^{12}C +^{208}Pb, ^{16}O+^{64}Zn, and ^{16}O+^{208}Pb systems have been analyzed at energies close to the Coulomb barriers. The optical potential parameters were obtained by fitting both fusion and elastic scattering data. Full Coupled-Channel (CC) code, which involves the Continuum-Discretized-Coupled-Channels (CDCC) framework, has been employed to perform the calculations. The calculations are cross-sections σ_{fusion}, barrier distribution D_{fusion} and tunneling probability P_{fusion} for fusion. As well as the elastic cross section to the Rutherford cross section $\sigma_{elastic}/\sigma_R$ with angle center of mass θ_{cm}, and energy center of mass E_{cm} and the barrier distribution of elastic scattering $D_{elastic}$ with energy center of mass E_{cm}. The results show that the fusion reaction cross section σ_{fusion} for the system ^{12}C +^{208}Pb do not agree with the experimental results down to the height of the Coulomb barrier V_b and the results in elastic scattering and fusion calculations are in better agreement with the experimental data. To provide a broader theoretical foundation for the optical potential, we discuss several alternative formalisms including the microscopic double folding and energy density approaches, the extended Thomas Fermi (ETF) method with Skyrme forces, and dispersive or extended optical model (EOM) frameworks that incorporate Ginocchio type phenomenology. These models help explain the observed energy dependence and demonstrate that the phenomenological Woods Saxon potential used in this work is consistent in magnitude and diffuseness with the predictions of microscopic and semi microscopic theories.

Keywords: Elastic scattering; Coulomb barrier; Barrier distribution; Coupled Channels; Tunneling Probability

1. Introduction

The distribution of potential barriers arises from the coupling to direct reaction channels. This distribution has a significant influence on the dynamics of heavy ion fusion and elastic scattering near the Coulomb barrier energy [1]–[3]. The influences of channel coupling, or on the potential model [1],[4],[5]. Basically, nucleon scattering is the most convenient and easier method for determining a nucleus' potential and/or its structure. As a result, the measurement of elastic scattering and the couplings of relative motion between impacting nuclei related to their intrinsic motion, in massive ion impacts at the Coulomb barrier, in addition to transfer processes, have long been understood.

The effects of Channel coupling significantly increase the cross sections in fusion reactions of heavy ion events at sub-barrier energies, compared to calculations based reactions, added to the total reaction cross sections at low energies, could be highly relevant to an elaborate theoretical approach [6],[7]. Total-elastic scattering, which includes three processes, is elastic or inelastic with transfer in reverse angles, and can provide analogous details such as the fusion cross section [8]–[10].

To obtain an exemplification of the barrier distribution, measuring total-elastic cross sections instead of the cross sections of fusion has some empirical attractiveness [11],[12].

These are: (a) the first derivative of practical values is taken with less precision instead of the second derivative, (b) unlike mensuration of the fusion cross section, which necessitates to determine defection separators (electrostatic deflector/ velocity filter) with low approval and competence, measuring σ_{fusion} requires only the use of quite simple charged-particle detectors, which may not have good energy or charge resolution, and (c) since each angular momentum exist scattering angle corresponds to specified cross sections in the semiclassical approximation by taking into consideration the centrifugal correction, for some active energies can be determined at a single ray [11].

The impact of coupling in channels (CC) has been considered in the theoretical description of fusing nuclei by tunneling through the Coulomb barrier, as coupling increases the cross sections in the sub-barrier region. In the frame of CC results, a considerable number of empirical data were appropriately explained [13]. Hussain *et al.* were studied using both quantum and semiclassical techniques; the pairing influence between the break-up channel and the elastic channel was investigated using the Continuum Discretized Coupled Channels (CDCC) method in Ref. [14].

The (CC) program was used to determine the fusion calculations, which included σ_{fusion}, D_{fusion}, P_{fusion}, and <L> by quantum mechanics in Refs. [15],[16]. However, the effects of coupled channels in heavy-ion reactions on cross-section, barrier distribution, and fusion probabilities with the polar orientation were discussed, as referenced in [17],[18].

Central ingredient of coupled channels analyses is the complex optical potential (real plus imaginary). Traditionally, Woods Saxon forms are adopted and their parameters are adjusted to reproduce elastic angular distributions, reaction cross sections, and fusion excitation functions.

However, several complementary theoretical frameworks have been developed to derive or constrain the nucleus interaction more microscopically. Microscopic and semi microscopic approaches, including the double folding and energy density approximations, construct the real part of the potential directly from effective nucleon-nucleon interactions folded with projectile and target densities; these treatments incorporate exchange and Pauli blocking effects and yield realistic short range repulsion and surface properties [19]-[21].

The extended Thomas Fermi (ETF) method with Skyrme forces refines this picture by expanding the kinetic energy density to $O(\hbar^2)$, with gradient and spin double folding and energy density formalisms the real part arises from folding effective NN interactions with projectile and target densities: orbit terms that reproduce barrier heights and curvatures across many systems. On the phenomenological side, extended optical model (EOM) formulations separate direct and fusion polarization potentials and link the energy dependence of real and imaginary components through dispersion relations; analytically tractable Ginocchio type potentials have also been used to interpret threshold anomaly and fusion hindrance near the barrier [22]–[24].

The aim of the research is to analyze coupled-channels in $^{12}C + ^{208}Pb$, $^{16}O + ^{64}Zn$, and $^{16}O + ^{208}Pb$ reactions, which studies the dynamics of fusion and scattering reactions by utilizing a full quantum mechanics (CC) Code. Involved the Continuum-Discretized Coupled Channels (CDCC) method of Alder and Winther (AW) theory.

This method takes into account Coulomb excitations that have been utilized in calculations of fusion and scattering reactions.

We determine optical model parameters by simultaneous consideration of elastic and fusion data. In parallel with the phenomenological parameter extraction, we discuss how the adopted Woods Saxon scales compare with microscopic folding/ETF expectations and with the dispersive trends that relate real and imaginary part of potential.

2. Theoretical Consideration

2.1. Equations

Reaction processes of inactive nuclei in heavy ion, the projectile's incoming flux is flexibly scattered or collected from the target nucleus. There is no correlation between angular momentum and energy in the region of optical potential.

The cross sections of absorption are associated with the cross sections of fusion if the fictional part of the optical potentials is powerful appropriate and located fully within the Coulomb barrier [12],[25]. The cross sections of total fusion and elastic reaction dependent on degree of freedom of Schrödinger equation in the projectile-target nuclei.

The elastic channel is affected in channel coupling by the complex part of energy potential [26],[27]:

$$V_t^{opt}(r) = V^{opt}(r) - iW^{opt}(r) \qquad (1)$$

$V^{opt}(r)$ is the real part given by,

$$V^{opt}(r) = V_N(r) + V_C(r) \qquad (2)$$

$V_N(r)$ is a short-range nuclear potential, $V_C(r)$ is a long-range Coulomb potential between projectile-target nuclei.

$W^{opt}(r)$is imaginary part short range for the input flux dissipated by activated channels. In microscopic with density dependence and exchange terms

$$V_{DF}(R) = \int \rho_P(r_P)\rho_T(r_T)v_{eff}$$

$$(|r_P - r_T + R|)d^3r_Pd^3r_T$$

introducing Pauli and kinetic energy effects consistent with nuclear matter properties [21]. The ETF method with Skyrme forces further includes $\hbar 2$ gradient and spin orbit corrections to the kinetic energy density, improving surface thickness and barrier curvature predictions [19].

The EOM treatments one writes $V_t\,(r;\,E) = V\,(r;\,E) + iW\,(r;\,E)$ with energy dependent components constrained by dispersion relations linking ΔV (E) to $W\,(E)$; this ensures causal consistency and captures channel coupling polarization effects [20].

Phenomenological Ginocchio type potentials provide an analytically solvable form whose real imaginary interplay reproduces threshold anomaly and aspects of fusion hindrance near the barrier [22]. The mechanism of reactions is given by the Schrödinger equation [28];

$$T + V^{opt}(r) - iW^{opt}(r)\psi^{(+)}(r) = E\psi^{(+)}(r) \qquad (3)$$

The relative motion is represented by T, the kinetic energy operator between the projectile target, while E denotes its energy.

One may express the wave function as follows [29];

$$\psi^{(+)}(r) = \varphi_c + \psi^{(sc)}(k;r) \qquad (4)$$

here, k represents the incident wave vector, φ_c signifies the wave function for Coulomb scattering in its unadulterated state (by establishing $V_N = W^{opt.} = 0$), and $\psi^{(sc.)}$ indicates the modification of the scattered wave due to V_N and W^{opt}.

The boundary conditions of the scattering are achieved by wave functions [27],[30].

$$\varphi_c(k;r,z)_{|r\to z|\to\infty}\frac{1}{(2\pi)^{\frac{3}{2}}}$$

$$[\exp ikz - i\eta\, ln\big(k(r-z)\big) + \qquad (5)$$

$$f_C(\theta)\frac{\exp i(kr - \eta\, ln2kr)}{r}]$$

$$\psi^{(sc)}(k;r)_{r\to\infty}$$

$$\frac{1}{(2\pi)^{\frac{3}{2}}}\left[f_N(\theta)\frac{\exp i(kr - \eta\, ln2kr)}{r}\right] \qquad (6)$$

where $f_C(\theta)$ is the Coulomb scattering amplitude, and $f_N(\theta)$ is the nuclear scattering intensity linked to the contact at short distance.

The equation uses the scattering amplitudes to determine the cross sections of elastic scattering [30].

$$\frac{d\sigma}{d\Omega} = |f_C(\theta) + f_N(\theta)|^2 \qquad (7)$$

The Hamiltonian is not Hermitian because of the imaginary portion of the optical potential, and as a result, the continuity equation is not achieved. In other words, the stationary wave function's related divergence of the current does not disappear. We acquire the updated expression by following the standard procedures to derive the continuity equation [29];

$$\nabla.\mathfrak{I} = -\frac{2}{\hbar}W^{opt}(r)\left|\psi^{(+)}(r)\right|^2 \qquad (8)$$

$\psi^{(+)}$ constitutes the solution of Eq. (3) under the boundary conditions pertinent to the scattering process, and $\mathfrak{I}$ represents the probability density current [29];

$$\mathfrak{I} = \frac{\hbar}{2\psi\mu i}\left[(\psi^{(+)})^*\nabla\psi^{(+)} - \psi^{(+)}\nabla\big(\psi^{(+)}\big)^*\right] \qquad (9)$$

By employing the Gauss-theorem and the definition of the absorption cross section, we may integrate the previously indicated equation over a sphere of radius R approaching infinity to derive [31];

$$\sigma^A = \sigma^R = (2\pi)^3\frac{k}{E}\left\langle\psi^{(+)}\middle|W^{opt}\middle|\psi^{(+)}\right\rangle \qquad (10)$$

In direct reactions, both cross sections of the fusion and the total scattering are represent by the formula [29];

$$\sigma_{fusion} = (2\pi)^3\frac{k}{E}\left\langle\psi^{(+)}\middle|W^{fusion}\middle|\psi^{(+)}\right\rangle \qquad (11)$$

$$\sigma_D = (2\pi)^3\frac{k}{E}\left\langle\psi^{(+)}\middle|W^{D}\middle|\psi^{(+)}\right\rangle \qquad (12)$$

One performs partial-wave expansions for practical reasons. When spins are disregarded, the statements above become [29],[31];

$$\sigma_{fusion} = \frac{\pi^2}{k}\sum_l (2l+1)\,T^{fusion} \qquad (13)$$

$$T_l^{fusion} = \frac{4k}{E}\int dr\,W^{fusion}\,(r)|u_l(k;r)|^2 \qquad (14)$$

with

$$\sigma_D = \frac{\pi^2}{k}\sum_l (2l+1)\,T^D \qquad (15)$$

with

$$T_l^D = \frac{4k}{E}\int dr\,W^D\,(r)|u_l(k;r)|^2 \qquad (16)$$

The radial equation originating from the origin is numerically integrated to obtain the wave function, $u_l(k;\ r)$ with the condition $u_l(k;\ 0)\ =\ 0$.

The initial value of the derivative just influences the overall normalization, allowing for arbitrary selection [29].

An alternate mode to estimate the radial part of wave function is to utilize an Ingoing Wave Boundary Condition ($IWBC$) [32]–[34].

This mode is explained that the elastic cross sections in a heavy-ion reaction is independent of the specifics of the optical potential at close ranges forms. Due to the intense absorption, it is sensible to suppose that at part of entering radius R_0, shorter than the barrier radius, R_b, It reduces the wave function to its entering part. The derivative of a logarithm of $u_l(k;r)$ is provided by [27];

$$\frac{du_l(k;r)}{dr} = -\frac{\frac{dk_l}{dr}}{2k_l^2} - ik_l(r) \qquad (17)$$

Eqs. (13) and (14) are now presented in an analogous form that is more suited for approximations.

We suppose that fusion absorption is the only source of the imaginary potential.

A more general situation will be Substituting Eq. (8) into Eq. (11), we get [27];

$$\sigma_{fusion} = \frac{(2\pi)^3}{v}\int(-\nabla.\mathfrak{J})d^3r \qquad (18)$$

where the current of Eq. (19) is denoted by $\mathfrak{J}$ and the asymptotic notation of relative velocity is given by $v = \frac{\hbar\,k}{\mu}$. The region where $W^{fusion}\ (r)$ is relevant is included in the integration, which takes place within a sphere with radius R_{fusion} [35].

By integrating over the same sphere's surface in accordance with the divergence theorem, we may find the cross section.

The cross section is determined via an integral across the surface of the same sphere using the divergence theorem.

$$\sigma_{fusion} = \frac{(2\pi)^3}{v}\int_{\wp}(-\hat{r}.\mathfrak{J})ds$$
$$= \frac{(2\pi)^3}{v}\int d\Omega(-\hat{r}.\mathfrak{J}) \qquad (19)$$

In above equation, $\hat{r}$ is the radius unit vector, which in the specified direction relates to the norm to spherical surface's by $\Omega(\equiv\ \theta,\phi)$.

Since $\left(\vec{\nabla} = -\partial\hat{r}/\partial r - ir * L\right)$ [35], can be write;

$$\hat{r}.\mathfrak{J} = \frac{\hbar}{2\mu i}\left[(\,\psi^{(+)})^*\frac{\partial\psi^{(+)}}{\partial r} - \psi^{(+)}\ \frac{\partial(\psi^{(+)})^*}{\partial r}\right] \qquad (20)$$

Apply the partial-waves expansion now [36];

$$\psi^{(+)}(k;r) = \frac{1}{(2\pi)^{3/2}}\sum_l(2l+1) \qquad (21)$$
$$P_l(cos\theta)i^l \exp i\sigma_l\frac{u_l(k;r)}{kr}$$

In Eq. (19) and add the outcome in Eq. (20). We determine Eq. (13) with the fusion probability applying the Legendre Polynomials by orthogonality relationship. provided by [36];

$$T_l^{fusion} = \frac{\mathfrak{J}_l^{fusion}}{-v/4} \qquad (22)$$

Above, $[\mathfrak{J}_l^{fusion} = \mathfrak{J}_l(R_{fusion})] \equiv$ is the radial current.

$$\mathfrak{J}_l(r) = \frac{\hbar}{2\mu\,i}\{(u_l(k;r))^*\frac{du_l(k;r)}{dr} -$$
$$u_l(k;r)\frac{d[u_l(k;r)]^*}{dr}\} \qquad (23)$$

Valuation at $r = R_{fusion}$. The drawback of Eq. (22) invalid for any normalization of the radial-wave function, it should be noted.

This results from the specific forms of Eqs. (5), (6) and (21). It is appropriate to obtain definition that is not affected by normalization [36].

For this reason, we get u_l as the sum;

$$u_l(k;r) = u_l^{(-)}\ (k;r) + u_l^{(+)}\ (k;r) \qquad (24)$$

The radial equation with input and output boundary conditions $r\to\infty$, and the values of $u_l^{(-)}$ and $u_l^{(-)}$ are solutions to this equation.

The approximate forms are used for the dependant normalization [37].

$$u_l^{(-)}\ (k;r\to\infty\ ) =$$
$$\frac{i}{2}\exp\left[-i\left(kr - \frac{l\pi}{2} - \eta\ ln(2\rho) + \sigma_i\right)\right] \qquad (25)$$

$$u_l^{(+)}\ (k;r\to\infty\ ) =$$
$$\frac{i}{2}\ \bar{S}_l\exp\left[i\left(kr - \frac{l\pi}{2} - \eta\ ln(2\rho) + \sigma_i\right)\right] \qquad (26)$$

where $\bar{S}_l$ represents the S-matrix escorted of the nuclear potentials. for the state, entering and outcome current intensity may be extracted by apply of $u_l^{(-)}$ and $u_l^{(+)}$ in Eq. (23), in sequence. The entering current intensity is appeared by [37]

$$\mathfrak{J}_l^{in} = \lim_{r\to\infty}\mathfrak{J}_l^-(r) = \frac{\hbar}{2\mu\ i}$$
$$\lim_{r\to\infty}\left[\left(u_l^{(-)}\right)^*\frac{du_l^{(-)}}{dr} - u_l^{(-)}\frac{\left(u_l^{(-)}\right)^*}{dr}\right] \qquad (27)$$

Inserting Eq. (25) into Eq. (27) at r→∞ limits we get [37] ;

$$\Im_l^{in} = -\frac{v}{4} \tag{28}$$

Utilizing this outcome, Eq. (22) gets the shape [37];

$$\Im_l^{fusion} = \frac{\Im_l^{fusion}}{\Im_l^{in}} \tag{29}$$

Considerably, the imaginary part of potential escorted with absorption process in fusion is defined through a $Woods - Saxon$ potential and a slight radius, R_{fusion}, and small pervasively.

If one supposes that $IWBC$ may be utilized at $R_{fusion} \cong R_0$, $\Im_l^{fusion}$ able to valuate applying $u_l^{(-)}(k;r)$ in Eq. (28). we get [12], [37];

$$\sigma_{fusion}^{cl} = \pi R_b^2 \left(1 - \frac{V_b}{E}\right) \theta(E - V_b) \tag{30}$$

The height of barrier is represented by V_b. And

$$\sigma_{elastic}^{cl} = \sigma_R(E, \pi) \theta(E - V_b) \tag{31}$$

The $\sigma_R(E,\pi)$ is the cross section of Rutherford. The ratio $\sigma_{elastic}^{cl}/\sigma_R$ is the reflection probability in classical framework $R(E) = 1 - T_{fusion}$ [38], [39].

The elastic scattering differential cross sections at θ° are represent in Eq. (30) of the classical framework of pure state, in a forceful Coulomb potential.

The coupled-channels equations are given by:

$$\Big(-\frac{\hbar^2}{2\mu}\frac{d^2}{dr^2} + \frac{j(j+1)\hbar^2}{2\mu\, r^2} +$$

$$V_0(r) - E + \epsilon_i\Big)\; u_i(r) + \tag{32}$$

$$\sum_i \sqrt{\frac{2\lambda + 1}{4\pi}} f(r) \langle \phi_{i_0} | T_{\lambda_0} | \phi_{\acute{\iota}_0} \rangle u_{\acute{\iota}}(r) \; = 0$$

where $|\phi_{i_0}\rangle$ is a representation of an intrinsic wave function that generated $H_{in}\,|\phi_{i_0}\rangle = \epsilon_i\,|\phi_{i_0}\rangle$. It is assumed that the Hamiltonian is present when coupled, as denoted by $V_{coup.} = f(r)\Upsilon_{\lambda\mu}(r)\hat{T}_{\lambda\mu}^{*}(\xi)$.

To solve the coupling equations for the channels, the boundary conditions of scattering for $u_i(r)$ can be employed [11], [32];

The $H_j^{(-)}(k_s r)$ is entering and the $H_j^{(+)}(k_i r)$ outgoing functions of Coulomb wave. The wave number of channel k_i is given by $\sqrt{2\mu(E-\epsilon_i)/\hbar^2}$ and $k_i = k_{i_s} = 2\mu E/\hbar^2$ and $\bar{S}_i^j$ is the nuclear S matrix. The angular distribution of scattering in the channel i which is indicated by [10];

$$\frac{d\sigma_i}{d\Omega} = \frac{k_i}{k_s} |f_i(\theta)|^2 \tag{34}$$

and

$$f_i(\theta) = \sum_j e^{i[\sigma_j(E) + \sigma_j(E - \epsilon_i)]} \tag{35}$$

$$\sqrt{\frac{2j+1}{4\pi}}\, \mathbb{Y}_{j0}(\theta) \frac{-2i\pi}{\sqrt{k_s k_{li}}}$$

$$\left(\bar{S}_i^j - \delta_{i,i_s}\right) + f_c(\theta)\delta_{i,i_s}$$

where $\sigma_j(E)$ is the phase shift of Coulomb potential. From the limits of $\epsilon_i \longrightarrow 0$, the coupling channels are abbreviated in Eq. (32) completely break up. The coupling matrix defined in this limit, as [39];

$$V_{i\acute{\iota}} = \epsilon_i \delta_{i\acute{\iota}} + \sqrt{\frac{2\lambda + 1}{4\pi}} f(r) \langle \phi_{i_0} | T_{\lambda_0} | \phi_{\acute{\iota}_0} \rangle \tag{36}$$

The $\sigma_R(E,\pi)$ is the cross section of Rutherford. The ratio $\sigma_{elastic}^{cl}/\sigma_R$ is the reflection probability

$$\sigma_{fusion}(E) = \sum_\beta G_\beta\, \sigma_{fusion}^{(\beta)}(E) \tag{37}$$

$$\sigma_{total}(E,\theta) = \sum_i \sigma_i\,(E,\theta)$$

$$= \sum_\beta G_\beta\, \sigma_{elastic}^{(\beta)}(E,\theta) \tag{38}$$

where $\sigma_{fusion}^{(\beta)}(E)$ and $\sigma_{elastic}^{(\beta)}(E,\theta)$ are cross sections of the fusion with the elastic for a potential in the eigen-channel β, which is, $V_\beta(r) = V_0(r) + \lambda_\beta(r)$. Here, $\lambda_\beta(r)$ indicated to eigen-value of the matrix in coupled state as Eq. (36) [when $\epsilon_i = 0$, $\lambda_\beta(r)$ is easy defined by $\lambda_\beta(r).f(r)$]. The weight factor G_β is given by $G_\beta = U_{0\beta}^2$, where U is considered the diagonalize unitary matrix [39], [40].

The effect of the coupling channels can be described explicitly within the Continuum-Discretized Coupled Channels (CDCC) framework.

The CDCC method quantum mechanical, which was originally developed to investigate the influence of deuteron breakdown on elastic scattering, has been extensively used to investigate heavy-ion reactions caused by light weak coupled nuclei.

The CDCC results have previously been succeeded in explained deuterons scattering on various targets. The typical three-body CDCC approach was also utilized to total fusion processes, yielding significantly good absorption cross sections from those obtained using optical model matches to elastic scattering empirical values [13].

3. Distributions of Coulomb Barrier

The accuracy of fusion data and coupled-channels computations have demonstrated that barrier distributions of fusion, $D_{fusion} = d^2[E\sigma_{fusion}]/dE^2$, is dependent on the specifics of the channel couplings, whereas the fusion cross sections make the sensitivity more harder [41].

Total elastic scattering (a combination of elastic with inelastic, and transfer interactions) at back angles can provide an analogous input as the fusion cross section [9], [41].

As an equivalent formulation of the barrier distribution, the ratio's first derivative of total elastic to cross sections of Rutherford, $d\sigma_{total}/d\sigma_R$, in relative to the energy E, i.e., $D_{total} = -d(d\sigma_{total}/d\sigma_R)/dE$ was used [12]. Then the barrier distribution equations are given by;

$$\sigma_{fusion}(E) = \sum_{\beta} G_\beta\, \sigma_{fusion}^{(\beta)}(E) \tag{39}$$

$$= \sum_{\beta} G_\beta\ \pi\, R_C^2 B_{fusion}^{\beta}\ (E)$$

$$D_{elastic} = -\frac{d}{dE}\left(\frac{d\sigma_{total}}{d\sigma_R}\ (E,\pi)\right) \tag{40}$$

$$= \sum_{\beta} G_\beta\, B_{elastic}^{\beta}\ (E)$$

The distributions D_{fusion} and $D_{elastic}$ provide more details regarding the height and location of the barrier. Through the emergence of potential structure, they would also provide a measurement of the strength of coupled channels actions in both D_{fusion} and $D_{elastic}$.

4. Results and discussion

The analysis of fusion and elastic scattering experimental values through the quantum mechanics calculations are implemented by coupled channels program which is called (CC) Code. The coupled channels calculations have been achieved for ^{12}C+^{208}Pb, ^{16}O +^{64}Zn and ^{16}O+^{208}Pb systems by using the CDCC method. The parameters of nuclear potential (Woods-Saxon) in parts (real and imaginary) are extracted by this Code that works with fusion and scattering reactions as listed in Table. 1 and 2. But the extracted scales (depths and a_r) are compared a posteriori with microscopic expectations. In particular, we find a_r values in the range 0.6–0.95 fm, consistent with the 0.8–1.0 fm range from ETF analyses, while the moderate energy dependence in $W(E)$ aligns qualitatively with dispersive constraints.

Table 1. The parameters of nuclear potential in (real and imaginary parts) and peak height of barriers used in calculations of fusion

Systems	V_r (MeV)	r_r (fm)	a_r (fm)	W_i (MeV)	r_i (fm)	a_i (fm)	V_b (MeV)
^{12}C+^{208}Pb	82.2	1.09	0.93	27.4	0.957	0.766	57.62
^{16}O +^{64}Zn	84.7	1.20	0.60	28.2	0.964	0.762	33.0
^{16}O+^{208}Pb	210.3	0.93	0.95	70.1	0.974	0.755	76.63

Table 2. The parameters of nuclear potential in (real and imaginary parts) of barrier applied in calculations of elastic scattering

Systems	V_r (MeV)	r_r (fm)	a_r (fm)	W_i (MeV)	r_i (fm)	a_i (fm)	$E_{c.m.}$ (MeV)	$\theta_{c.m.}$ (deg)
^{12}C+^{208}Pb	272.9	1.10	0.63	91.0	0.957	0.35	66.1	99
^{16}O +^{64}Zn	62.0	1.20	0.63	20.7	1.25	0.45	38.3	61
^{16}O+^{208}Pb	225.8	1.10	0.63	85.3	1.25	0.51	83.57	105

4.1. ^{12}C+^{208}Pb System

In the ^{12}C+^{208}Pb system, the results of this reaction consist of the ^{12}C as a stable nucleus and the target ^{208}Pb is heavy ion are taken the cross section σ_{fusion} and barrier distribution D_{fusion} with tunneling probability P_{fusion} in Fig. 1, parts A, B and C, in sequence. The elastic cross sections to the Rutherford cross section $\sigma_{elastic}/\sigma_R$ are specified for angle of center mass θ_{cm} (Fig. 2, part A), and energy E_{cm} (in Fig. 2, part B) with best-fit parameters as in Table. 1 and 2. The barrier distribution of elastic scattering $D_{elastic}$ is specified with energy of center mass E_{cm} (in Fig. 2, part C). The results of D_{fusion} with P_{fusion} above barrier in good correspondence with experimental data [42], for coupled and no coupled state as shown the chi square χ^2 values above and below barrier in Table. 3.As for the values of σ_{fusion} at high energies above the Coulomb barrier, a clear discrepancy is observed between the theoretical calculations and the experimental values [42], whereas a reasonable agreement is noted below the barrier. When comparing our results with previous theoretical calculations from the same source [42], both sets of calculations are consistent with the experimental values above the barrier. However, the previous calculations deviate from ours to match the experimental data at sub-barrier energies. This discrepancy in energies above the barrier is attributed to the calculations' absence of coupling to vibrational states and nuclear potential transitions, it also contributes to the loss of the incident flux when the two nuclei collide, as it is diverted to other channels such as nucleon transfer and others. In addition, since the system is heavy, it requires sufficient energy to overcome the Coulomb barrier for fusion to occur. Otherwise, it creates a hindrance to fusion, which leads to a reduction in the experimental values. In contrast, below the barrier, the inclusion of such couplings leads to better agreement with the experimental values in both our results and the previous ones. The barrier height was determined by a good fit to the experimental cross-section data using the (CC) code. The resulting barrier height is $V_b = 57.62$, which corresponds to the $V_r = 82.2$, $r_r = 1.09$ and $a_r = 0.93$, which differ from the previous calculations where V_b= 57.0 MeV with $V_r = 87.0$, $r_r = 1.07$ and $a_r = 0.95$. For the elastic distribution of barrier, the correspondence will be further ameliorated above barrier. The $\sigma_{\text{elastic}}/\sigma_{\text{R}}$ of scale of angle θ_{cm} very matches in range θ_{cm} =90-130 with data, but $\sigma_{\text{elastic}}/\sigma_{\text{R}}$ of scale of angle E_{cm} in that rapprochement with experimental data [43] above barrier for no available data below barrier (in Fig. 2, panel B and C).

In order to analyze the collision information and derive a uniform accurate representation and observation cross sections of elastic scattering and fusion reactions. The results were determined for the $^{12}C+^{208}Pb$ reaction using the same formula and potential. Also, it used to investigate the unusual peak form in the barrier distribution of function's fluctuation. When compared with previous calculations, as shown in Fig. 2, panel A, a noticeable deviation is observed between our results and the experimental values. However, the earlier calculations [42],[44] exhibit better agreement with the experimental data at large scattering angles. This agreement at wide angles can be attributed to the loss of flux from elastic scattering channels toward the steep gradient associated with large-angle deflection. In contrast, at smaller angles within the range of 70°–90°, both calculations coincide, although the earlier calculations slightly overestimate the experimental data. The agreement between the theoretical and experimental results for elastic scattering is more clearly evident through the chi-square values in Table. 4. The values were taken for the cross-sections as a function of energy and the barrier distribution over the entire barrier due to the limited number of experimental data points.

The diffuseness parameter employed in the fusion cross-section calculations was $a_r = 0.93$, while for elastic scattering, it was smaller, at $a_r = 0.63$. In previous studies such as [42], [44], varying a_r values were utilized, including 0.63, 0.95, and 0.55. The optimal value for describing fusion interactions was found to be $a_r = 0.95$, as reported in Section 3, Fig. 2A of [42]. The parameters adopted in that case were suited to fusion processes and thus differ from those required for elastic scattering, leading to the failure of such models to reproduce elastic scattering cross-sections when using $a_r = 0.95$.

Fusion reactions typically require a larger diffuseness parameter, unlike elastic scattering, which demands a smaller one. This distinction is primarily due to Fresnel diffraction effects, which persist even at large angles. The discrepancy in potential parameters between fusion and elastic scattering reactions could be attributed either to an unsuitable shape of the nuclear potential or to dynamic effects involving high partial waves. These high angular momentum components may result in significant overlap of the nuclear densities, which in turn inhibits the fusion process.

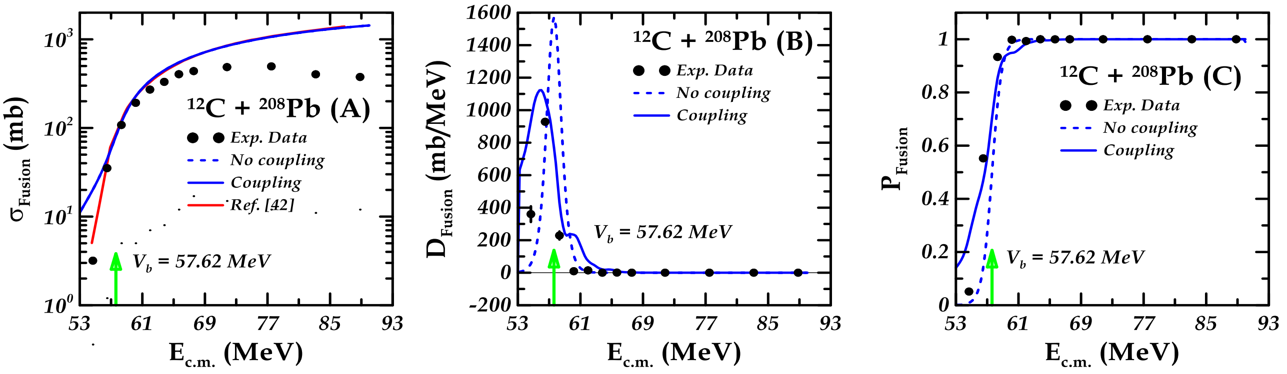

Figure 1. The first and second 2^+ (1.37, 4.238) MeV states' theoretical longitudinal form factors (a), (b) with various single potential and (c) different models compared to experiment results [8].

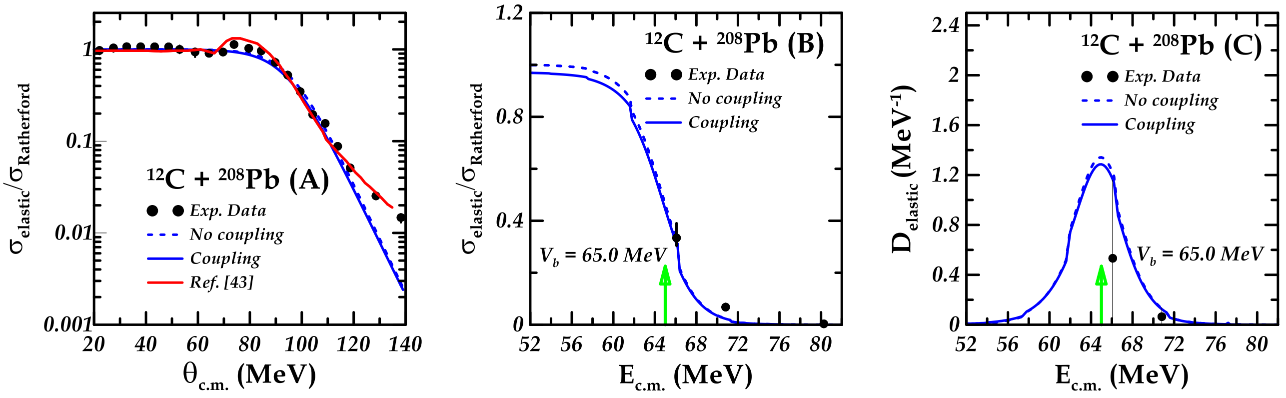

Figure 2. The calculations of uncoupled and coupled channels for $^{12}C+^{208}Pb$ by sporadic and continuous curves in sequence: Part (A) elastic cross sections of the Rutherford cross sections with θ_{cm} (blue color), part (B) elastic cross sections of the Rutherford cross sections with the energy E_{cm} (blue color), and part (C) the distributions of Coulomb barrier (blue color), the circles (black color) appear experimental points in Ref. [43]

4.2. ^{16}O +^{64}Zn System

The ^{16}O +^{64}Zn fusion is displayed as in Fig. 3, the calculations of total cross sections with distribution barrier and probability of fusion in panels (A, B, C) respectively. Several parameters have been dependent of potential in real and imaginary parts and height of barrier in fusion and scattering reactions as Tab. 1. The analysis of excitation cross sections as panel A, exhibits an excellent match to experimental data [45] around Coulomb barrier in a coupled state. Above barrier exhibit the match in no coupled state as well as a sharp fall in coupled state of below region Coulomb barrier.

The cross-section values were compared with previous theoretical values from reference [46], which were obtained using the (CCFULL) code. An excellent fit was achieved for both our calculations and the previous ones with the experimental values around the barrier. This is because the breakup channel does not significantly affect the fusion process, as the projectile is considered negligible in the breakup mechanism.

The analysis also shows an excellent match in the coupled case of tunneling probability in panel B, an acceptable match with practical values of the barrier distributions, as shown by the chi-square values in Table. 3.

The results of cross section in scattering interactions for angle of center mass θ_{cm} with energy of center mass E_{cm} to the cross sections of Rutherford $\sigma_{elastic}/\sigma_R$ is appear in Fig. 4, panels A and B.

The barrier distribution of elastic scattering $D_{elastic}$ is determined using the angle of mass center θ_{cm} with energy of center mass E_{cm} in part C. The coupling channels in all instructions are perfect agreement with experimental data [46]. We get bag splay in cross section of scattering to the cross section of Rutherford of θ_{cm} over angle $50^{\circ} - 90^{\circ}$ and E_{cm} at a sub-barrier region in no-coupling and coupled states. From reference [46], previous calculations of elastic scattering cross-sections were compared with our results. The theoretical values showed good agreement with the experimental data.

However, our calculations in the angular range of 50°–90° were lower than the experimental values, indicating that the diffuseness parameter of the imaginary potential is small $(a_r = 0.45)$. In contrast, the previous theoretical calculations used a larger value $(a_r = 0.63)$, which provided a better fit with the experimental data.

As well as elastic scattering barrier distribution $D_{elastic}$ calculations with E_{cm} down barrier responsible match with practical data from through Table. 4.

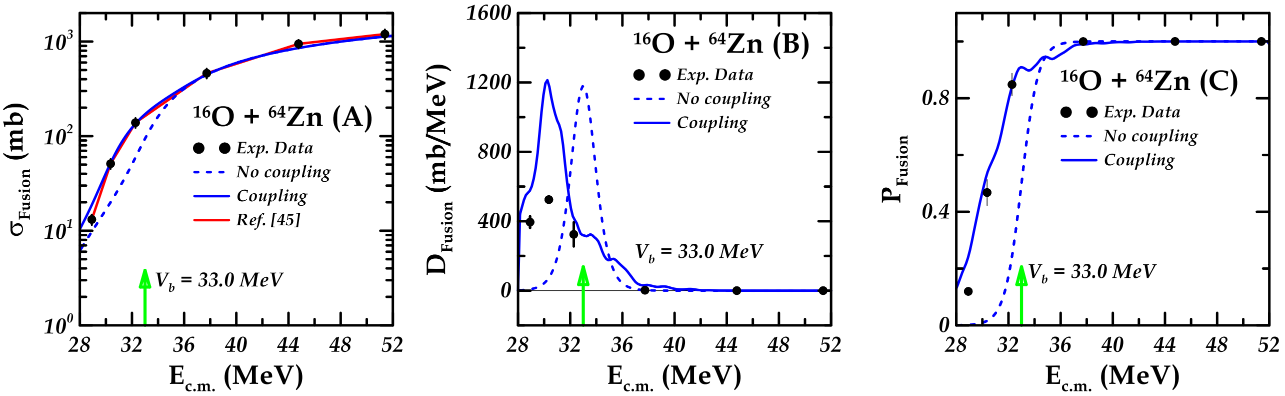

Figure 3. The calculations of uncoupled and coupled channels for ^{16}O+^{64}Zn by sporadic and continuous curves in sequence: Part (A) the cross sections of fusion (blue color), part (B) the distributions of Coulomb barrier (blue color), and part (C) tunneling probability, the circles (black color) appear experimental points in Ref. [45]

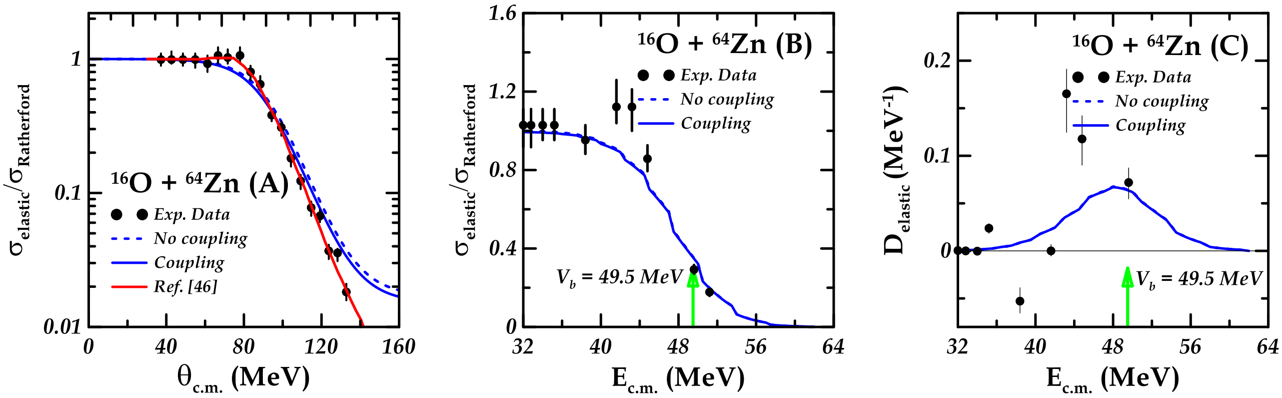

Figure 4. The calculations of uncoupled and coupled channels for ^{16}O+^{64}Zn by sporadic and continuous curves in sequence: Part (A) elastic cross sections of the Rutherford cross sections with θ_{cm} (blue color), part (B) elastic cross sections of the Rutherford cross sections with the energy E_{cm} (blue color), and part (C) the distributions of Coulomb barrier (blue color), the circles (black color) appear experimental points in Ref. [46]

4.3. $^{16}O+^{208}Pb$ System

projectile's inertial motion with the target greatly enhances calculations about the barrier. The barrier height energy was obtained through fitting the fusion cross-section data, yielding $V_b = 76.63\ MeV$. In contrast, reference [47] (Section 5C, Fig. 7A) adopted a higher barrier value of $V_b = 77.5\ MeV$, which resulted in different parameters. That study showed good agreement between the calculations and experimental data above and under the Coulomb barrier. A comparison was also made with previous calculations in reference [21], where different parameters were used in the coupling case. This led to a match with the experimental values both above and below the barrier energy. In our case, we adopted a single set of parameters for both coupled and uncoupled cases, based on the fitting to the fusion cross-section data. The little difference between the calculations is attributed to flux loss due to the reduced fusion process, as the (CCFULL) code in reference [21] included couplings for all orders of the nuclear potential. Our calculations are in excellent agreement with coupled state of the distribution in panel (B), and tunneling probability in panel (C) can be notice in Fig. 5, and chi values Table. 3. In this state, we used to set different parameters with height given 83.6 MeV which explain in order to clarify the elastic scattering. The parameter of diffuseness is less in imaginary part from real part and essential to understanding how described the behaver the cross sections of elastic scattering. The results of elastic scattering analysis can be noticed in Fig. 6. The effects considered of results give the best depiction of the experimental values [43] at the foreground and ending angles with cross $\sigma_{elastic}/\sigma_R$ as in panel (A) and are consistent with previous theoretical calculations from reference [43]. The results in panels (B) and (C) are given a reasonable agreement as shown in Table. 4 of chi square of the coupled channels with data above barrier. This indicating to the importance of role coupling channels.

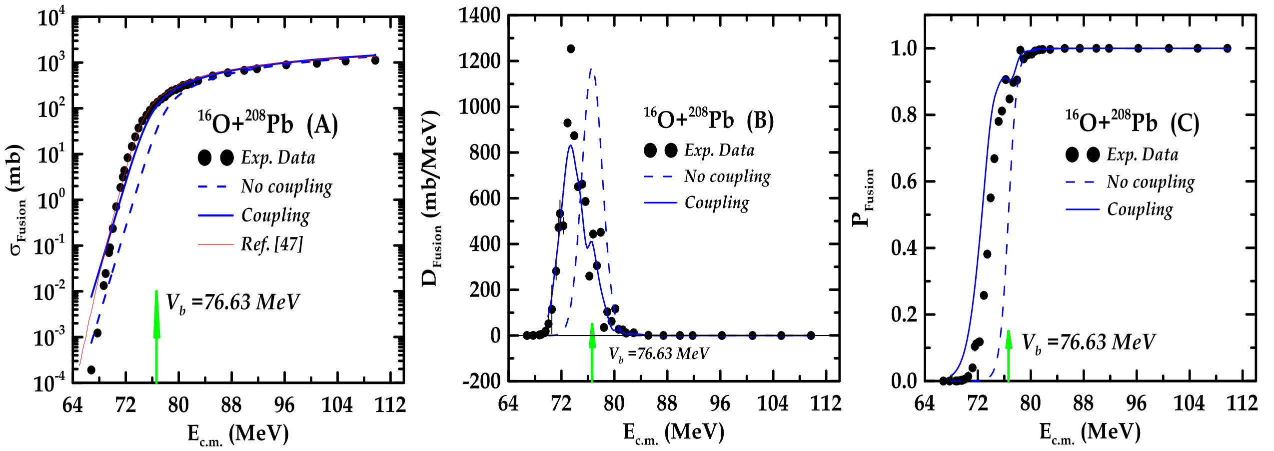

Figure 5. The calculations of uncoupled and coupled channels for $^{16}O+^{208}Pb$ by sporadic and continuous curves in sequence: Part (A) the cross sections of fusion (blue color), part (B) the distributions of Coulomb barrier (blue color), and part (C) tunneling probability, the circles (black color) appear experimental points in Ref. [47]

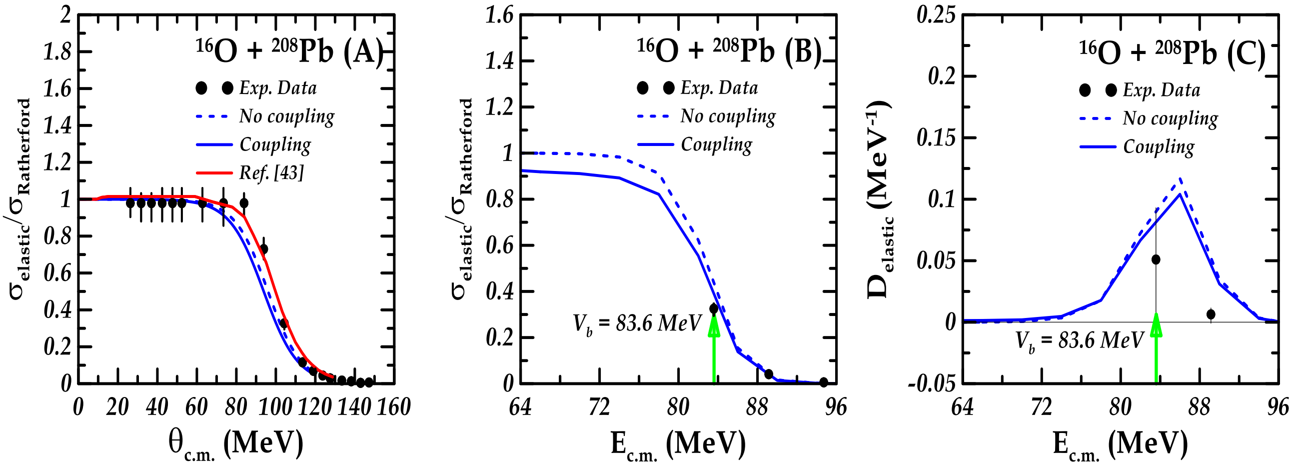

Figure 6. The calculations of uncoupled and coupled channels for $^{16}O+^{208}Pb$ by sporadic and continuous curves in sequence: Part (A) elastic cross sections of the Rutherford cross sections with $\boldsymbol{\theta_{cm}}$ (blue color), part (B) elastic cross sections of the Rutherford cross sections with the energy $\boldsymbol{E_{cm}}$ (blue color), and part (C) the distributions of Coulomb barrier (blue color), the circles (black color) appear experimental points in Ref. [43]

Table 3. The Chi square values of cross section, distribution and probability of fusion

System Channels	σ_{fusion}		D_{fusion}		P_{fusion}	
No coupling	χ^2above V_b	χ^2 under V_b	χ^2above V_b	χ^2 under V_b	χ^2above V_b	χ^2 under V_b
$^{12}C+^{208}Pb$	0.36682270	0.13146630	0.04583368	0.08509916	0.00301573	0.09757534
$^{16}O+^{64}Zn$	0.00334722	0.28977140	0.00063394	0.19402590	0.00000000	0.29253390
$^{16}O+^{208}Pb$	0.00023462	0.1977140	0.15433922	0.20433940	0.00001510	0.29253390
Coupling	χ^2above V_b	χ^2 under V_b	χ^2above V_b	χ^2 under V_b	χ^2above V_b	χ^2 under V_b
$^{12}C+^{208}Pb$	0.36682270	0.13146630	0.01942050	0.01846559	0.00072001	0.01257249
$^{16}O+^{64}Zn$	0.00332143	0.02998326	0.00024293	0.00406046	0.00000126	0.00096827
$^{16}O+^{208}Pb$	0.00001330	0.00031330	0.00043394	0.00001520	0.00000000	0.00000122

Table 4. The Chi square values of elastic cross sections of the Rutherford cross sections with θ_{cm} and E_{cm} and $D_{elastic}$

Systems	$\sigma_{elastic}/\sigma_R$ of θ_{cm}		$\sigma_{elastic}/\sigma_R$ of E_{cm}		$D_{elastic}$	
	No coupling	Coupling	No coupling	Coupling	No coupling	Coupling
$^{12}C+^{208}Pb$	0.250753	1.060833	0.166525	0.221307	0.05543588	0.01010523
$^{16}O+^{64}Zn$	0.33256520	0.19210300	0.23198010	0.03642063	0.88309900	0.52840410
$^{16}O+^{208}Pb$	0.16175000	0.05936645	0.04234848	0.02911760	0.08302087	0.08436900

We analyze $^{12}C+^{208}Pb$, $^{16}O+^{64}Zn$, and $^{16}O+^{208}Pb$ at near barrier energies. For each system, real and imaginary Woods Saxon parameters are adjusted to simultaneously reproduce elastic angular distributions and fusion excitation functions around the barrier. Coulomb and nuclear deformations, excitation energies, and coupling strengths follow standard systematics. A single parameter set is used for both fusion and elastic to test internal consistency; minor adjustments to a_r are noted where necessary. The relatively weak energy dependence of the imaginary part is compatible with dispersive optical model calculations that link $\Delta V(E)$ to $W(E)$ [20], and the moderate reduction of fusion probability below the barrier parallels the hindrance trends explained by Ginocchio based potentials [22]. Thus, while our potential is phenomenological, it effectively encodes the essential physical characteristics identified by microscopic and dispersive frameworks.

5. Conclusions

The analyses of fusion and scattering interactions were completed in terms of WS potential and full coupled channel (CC) code. The calculations were performed by CDCC method for tightly bound nuclei in $^{12}C+^{208}Pb$,$^{16}O+^{64}Zn$, and $^{16}O+^{208}Pb$ systems. We conclude that coupled-channels calculations give information about the mechanisms of important interactions in fusion and scattering. From the comparison, we can conclude that the cross sections of fusion with probability and elastic cross sections of the Rutherford cross sections are function angles and are described very well in the practical values. The fluctuations in peaks of the fusion barrier distribution and the energy scattering barrier distributions are satisfactorily characterized by our computed results. The findings derived from this research may prove beneficial for future heavy-ion collision studies. If explicitly situating our optical potential within microscopic (double folding, energy density, ETF) and dispersive/phenomenological (extended optical model, Ginocchio) formalisms, we demonstrate theoretical consistency of the adopted parameters. We conclude if implement microscopically constrained interactions derived from folding/ETF functionals within the CDCC workflow to reduce parameter ambiguity and provide a unified description of fusion and scattering data.

Authors Contribution
All authors conceived of the study, participated in its design and coordination, drafted the manuscript, participated in the sequence alignment, and read and approved the final manuscript.

Availability of data and materials
Not applicable. In fact, all results are obtained without any software and found by manual computations. In other words, the manuscript is in the pure mathematics (mathematical analysis) category.

Conflict of interests
The author states that there is no conflict of interest.

References

[1] N. Rowley, H. Timmers, J. R. Leigh, M. Dasgupta, D. J. Hinde, J. C. Mein, C. R. Morton, and J. O. Newton. Barrier distributions from elastic scattering. Phys. Lett. B, vol. 373, no. 1–3, pp. 23–29, Apr. 1996, https://doi.org/10.1016/0370-2693(96)00118-9

[2] W. Reisdorf, Heavy-ion reactions close to the Coulomb barrier. J. Phys. G Nucl. Part. Phys. vol. 20, no. 9, pp. 1297–1353, Sep. 1994,

https://doi.org/10.1088/0954-3899/20/9/004

[3] M. S. Gautam, S. Duhan, H. Kumar, Fusion of ^{40}Ca + ^{90,92,94,96}Zr combinations in near and sub-barrier domains. Indian J. Phys. vol. 97, no. 14, pp. 4383–4398, Dec. 2023, https://doi.org/10.1007/s12648-023-02799-5

[4] M. Beckerman, Sub-barrier fusion of two nuclei. Reports Prog. Phys. vol. 51, no. 8, pp. 1047–1103, Aug. 1988, https://doi.org/10.1088/0034-4885/51/8/001

[5] M. Zamrun F. and K. Hagino, Effects of anharmonic vibration on large-angle quasi-elastic scattering of $^{16\mathrm{O}+144}$Sm. Phys. Rev. C. vol. 77, no. 1, p. 014606, Jan. 2008, https://doi.org/10.1103/PHYSREVC.77.014606

[6] V. Soukeras, A. Pakou, F. Cappuzzello, L. Acosta, C. Agodi, N. Alamanos, M. Bondi, D. Carbone, M. Cavallaro, A. Cunsolo, M. De Napoli, A. Di Pietro, J. P. Fernández-García, P. Figuera, M. Fisichella, A. Foti, N. Keeley, G. Marquinez-Duran, I. Martel, M. Mazzocco, D. Nicolosi, D. Pierroutsakou, K. Rusek, O. Sgouros, E. Stiliaris, E. Strano, D. Torresi, Reexamination of 6Li+*p* elastic scattering in inverse kinematics. Phys. Rev. C. vol. 91, no. 5, p. 057601, May 2015, https://doi.org/10.1103/PhysRevC.91.057601

[7] W. G. Love, L. J.Parish, Tensor force formalism for inelastic scattering, charge exchange and knock-out reactions. Nucl. Phys. A. vol. 157, no. 2, pp. 625–645, https://doi.org/10.1016/0375-9474(70)90238-1

[8] Ş. Karatepe Çelik, İ. Boztosun, M. Doğru, An Analysis of Elastic Scattering Angular Distributions of ^{17} F on a ^{208} Pb Target at Different Energies. Few-Body Systems, vol. 62, no. 2, p. 14, Jun. 2021, https://doi.org/10.1007/s00601-021-01599-z

[9] M. V. Andres, N. Rowley, M. A. Nagarajan, Effect of deformation on the elastic and quasielastic scattering of heavy ions near the Coulomb barrier. Phys. Lett. B. vol. 202, no. 3, pp. 292–295, Mar. 1988, https://doi.org/https://doi.org/10.1016/0370-2693(88)90473-X

[10] K. A. Gridnev, N. A. Maltsev, N. V Leshakova, Effect of elastic and inelastic cluster transfer on elastic ^{16}O + ^{12}C and ^{16}O + ^{16}O scattering. Bull. Russ. Acad. Sci. Phys. vol. 77, no. 7, pp. 852–856, Jul. 2013, https://doi.org/10.3103/S1062873813070113

[11] N. Rowley, New Experimental Results on Emission and Reaction Barriers. Phys. Atom. Nuclei. vol. 66, no. 8, pp. 1450–1453, Aug. 2003, https://doi.org/10.1134/1.1601749

[12] K. Hagino, N. Rowley, Large-angle scattering and quasielastic barrier distributions. Phys. Rev. C. vol. 69, no. 5, p. 054610, May 2004, https://doi.org/10.1103/PhysRevC.69.054610

[13] C. Beck, N. Keeley, A. Diaz-Torres, Coupled-channel effects in elastic scattering and near-barrier fusion induced by weakly bound nuclei and exotic halo nuclei. Phys. Rev. C. vol. 75, no. 5, p. 054605, May 2007, https://doi.org/10.1103/PhysRevC.75.054605

[14] F. M. Hussain, F. A. Majeed, M. H. Meteab, Investigation of the Calculation of Coupled Channels for Some Halo Systems. Ukr. J. Phys. vol. 65, no. 11, pp. 951–957, Nov. 2020, https://doi.org/10.15407/ujpe65.11.951

[15] F. M. Hussain, F. A. Majeed, Quantum mechanical calculations of fusion reactions induced by multi-neutron halo systems below and above Coulomb barrier. Int. J. Nucl. Energy Sci. Technol. vol. 15, no. 1, pp. 23–35, 2021, https://doi.org/10.1504/IJNEST.2021.10043909

[16] M. Bhuyan, R. Kumar, Fusion cross section for Ni-based reactions within the relativistic mean-field formalism. Phys. Rev. C. vol. 98, no. 5, p. 054610, Nov. 2018, https://doi.org/10.1103/PhysRevC.98.054610

[17] F. M. Hussain, F. A. Majeed, Y. A. Abdul-Hussein, Enhanced calculations of fusion barrier distribution for heavy-ion fusion reactions using Wong formula. Int. J. Nucl. Energy Sci. Technol. vol. 13, no. 3, p. 226, 2019, https://doi.org/10.1504/IJNEST.2019.10024816

[18] L. Zhu, Z.-Q. Feng, C. Li, F.-S. Zhang, Orientation effects on evaporation residue cross sections in $^{48}\mathrm{Ca}$-induced hot fusion reactions. Phys. Rev. C. vol. 90, no. 1, p. 014612, Jul. 2014, https://doi.org/10.1103/PhysRevC.90.014612

[19] O. I. Davydovska, V. A. Nesterov, V. Y. Denisov, The nucleus-nucleus potential within the extended Thomas-Fermi method and the cross-sections of subbarrier fusion and elastic scattering for the systems ^{16}O + ^{58,60,62,64}Ni. Nucl. Phys. A. vol. 1002, p. 121994, Oct. 2020, https://doi.org/10.1016/j.nuclphysa.2020.121994

[20] E. F. Aguilera, F. Torabi, Optical Model description of fusion and elastic scattering of 6 Li + (58 Ni, 64 Zn) at sub-barrier energies. J. Phys. Conf. Ser. vol. 1078, no. 1, p. 012001, Aug. 2018, https://doi.org/10.1088/1742-6596/1078/1/012001

[21] O. I. Davydovska, V. Y. Denisov, V. A. Nesterov, Comparison of the nucleus-nucleus potential evaluated in the double-folding and energy density approximations and the cross-sections of elastic scattering and fusion of heavy ions. Nucl. Phys. A. vol. 989, pp. 214–230, Sep. 2019, https://doi.org/10.1016/j.nuclphysa.2019.06.004

[22] K. K. Jena, B. Sahu, J. K. Nayak, P. Raj Preethi, B. K. Sharma, and S. K. Agarwalla, "Simulations Study of Scattering and Fusion Hindrance Near Coulomb Barrier in F + Pb," *Acta Phys. Pol. B*, vol. 54, no. 4, pp. 1–9, 2023, https://doi.org/10.48550/arXiv.2307.05652

[23] M. Bhuyan, R. Kumar, S. Rana, D. Jain, S.K. Patra, B. V Carlson, Effect of density and nucleon-nucleon potential on the fusion cross section within the relativistic mean field formalism. Phys. Rev. C. vol. 101, no. 4, p. 044603, Apr. 2020, https://doi.org/10.1103/PhysRevC.101.044603

[24] B. Singh, M. Bhuyan, S.K. Patra, R.K. Gupta, Optical potential obtained from relativistic-mean-field theory-based microscopic nucleon–nucleon interaction: applied to cluster radioactive decays. J. Phys. G Nucl. Part.

Phys. vol. 39, no. 2, p. 025101, Feb. 2012, https://doi.org/10.1088/0954-3899/39/2/025101

[25] M. Al-abyad, H. E. Hassan, A. H. M. Solieman, F. Ditrói, Z. A. Saleh, Deuteron and α-particle-induced nuclear reactions on ^{45}Sc: activation cross section measurement and thick target yield evaluation. Indian J. Phys. vol. 97, no. 9, pp. 2787–2791, Aug. 2023, https://doi.org/10.1007/s12648-022-02574-y

[26] L. F. Canto, P. R. S. Gomes, R. Donangelo, J. Lubian, M. S. Hussein, Recent developments in fusion and direct reactions with weakly bound nuclei. Phys. Rep. vol. 596, pp. 1–86, Sep. 2015, https://doi.org/10.1016/j.physrep.2015.08.001

[27] L. F. Canto, P. R. S. Gomes, R. Donangelo, M. S. Hussein, Fusion and breakup of weakly bound nuclei. Phys. Rep. vol. 424, no. 1–2, pp. 1–111, Feb. 2006, https://doi.org/10.1016/j.physrep.2005.10.006

[28] W. Chen, D. Y. Pang, H. Guo, Y. Tao, W. Sun, Y. Ying, Continuum-discretized coupled-channels calculations for ^{6}Li fusion reactions with closed channels. Phys. Rev. C. 107(6), 64610 (2023). https://doi.org/10.1103/PhysRevC.107.064610

[29] [29] M. R. Cortes, V. A. B. Zagatto, J. L. Ferreira, J. Rangel, L. F. Canto, J. Lubian, Fusion reactions in ^{6}Li+^{90}Zr scattering. Phys. Rev. C. vol. 107, no. 6, p. 064610, Jun. 2023, https://doi.org/10.1103/PhysRevC.108.054601

[30] F. A. Majeed, F. A. Mahdi, Quantum mechanical calculations of a fusion reaction for some selected halo systems. Ukr. J. Phys. 64(1), 11 (2019). https://doi.org/10.15407/ujpe64.1.11

[31] C. Dash, R. R. Swain, G. Tripathy, I. Naik, B. B. Sahu, Scattering and fusion reaction dynamics of O+Zr system around Coulomb barrier. Chinese Phys. C. vol. 64, no. 1, pp. 11–18, Jan. 2019, https://doi.org/10.1088/1674-1137/ac92d9

[32] G. H. Rawitscher, Approximate Independence of Optical-Model Elastic Scattering Calculations on the Potential at Small Distances. Phys. Rev. vol. 135, no. 3B, pp. B605–B612, Aug. 1964, https://doi.org/10.1103/PhysRev.135.B605

[33] H. Feshbach, D. C. Peaslee, V. F. Weisskopf, On the Scattering and Absorption of Particles by Atomic Nuclei. Phys. Rev. vol. 71, no. 3, pp. 145–158, Feb. 1947, https://doi.org/10.1103/PhysRev.71.145

[34] G. H. Rawitscher, Ingoing wave boundary condition analysis of alpha and deuteron elastic scattering cross sections. Nucl. Phys. vol. 85, no. 2, pp. 337–364, Sep. 1966, https://doi.org/10.1016/0029-5582(66)90629-8

[35] J. D. Jackson, Classical Electrodynamics. Wiley, New York, 3rd edition (1975). [Online]. Available: https://www.wiley.com/en-us/Classical+Electrodynamics%2C+3rd+Edition-p-9780471309321

[36] J. C. Joachain and L. D. Roper, “Quantum Collision Theory,” *Phys. Today*, vol. 29, no. 12, pp. 53–53, Dec. 1976, https://doi.org/ 10.1063/1.3024665

[37] M. Abramowitz, I. S. Stegun, Handbook of Mathematical Functions. Dover Publications (1972). [Online]. Available: https://personal.math.ubc.ca/~cbm/aands/frameindex.htm

[38] H. Timmers, J. R. Leigh, M. Dasgupta, D. J. Hinde, R. C. Lemmon, J. C. Mein, C. R. Morton, J. O. Newton, N. Rowley, Probing fusion barrier distributions with quasi-elastic scattering. Nucl. Phys. A. vol. 584, no. 1, pp. 190–204, Feb. 1995, https://doi.org/10.1016/0375-9474(94)00521-N

[39] H. Esbensen, S. Landowne, C. Price, High-spin excitations in the rotating frame and sudden approximations. Phys. Rev. C. vol. 36, no. 6, pp. 2359–2364, Dec. 1987, https://doi.org/10.1103/PhysRevC.36.2359

[40] M. A. Nagarajan, N. Rowley, R. Lindsay, Adiabatic coupled-channels evaluation of inelastic scattering. J. Phys. G Nucl. Phys. vol. 12, no. 6, pp. 529–536, Jun. 1986, https://doi.org/10.1088/0305-4616/12/6/011

[41] F. Zamrun M., K. Hagino, Effects of anharmonic vibration on large-angle quasi-elastic scattering of ^{16}O+^{144}Sm. Phys. Rev. C. vol. 77, no. 1, p. 014606, Jan. 2008, https://doi.org/10.1103/PhysRevC.77.014606

[42] A. Mukherjee, D. Hinde, M. Dasgupta, J. Newton, R. Butt, K. Hagino, Failure of the Woods-Saxon nuclear potential to simultaneously reproduce precise fusion and elastic scattering measurements. Phys. Rev. C. vol. 75, no. 4, p. 044608, Apr. 2007, https://doi.org/10.1103/PHYSREVC.75.044608

[43] N. Wang, W. Scheid, Quasi-elastic scattering and fusion with a modified Woods-Saxon potential. Phys. Rev. C. vol. 78, no. 1, p. 014607, Jul. 2008, https://doi.org/10.1103/PhysRevC.78.014607

[44] Santra, S., P. Singh, S. Kailas, A. Chatterjee, A. Shrivastava, K. Mahata. Coupled reaction channel analysis of elastic, inelastic, transfer, and fusion cross sections for ^{12} C+ ^{208} Pb. Phys. Rev. C. vol. 64, no. 2, pp. 246021–2460214, Jun. 2001, https://doi.org/10.1103/PhysRevC.64.024602

[45] P. R. S. Gomes, T. J. P. Penna, R. Liguori Neto, J. C. Acquadro, C. Tenreiro, P. A. B. Freitas, E. Crema, N. Carlin Filho, kM. M. Coimbra, Nuclear fusion between heavy ions by the gamma-ray spectroscopy method. Nucl. Instruments Methods Phys. Res. Sect. A Accel. Spectrometers, Detect. Assoc. Equip. **vol.** 280, no. 2–3, pp. 395–401, Aug. 1989, https://doi.org/10.1016/0168-9002(89)90940-6

[46] P. R. S. Gomes, M. D. Rodríguez, G. V. Martí, I. Padron, L. C. Chamon, J. O. Fernández Niello, O. A. Capurro, A. J. Pacheco, J. E. Testoni, A. Arazi, M. Ramírez, R. M. Anjos, J. Lubian, R. Veiga, R. Liguori Neto, E. Crema, N. Added, C. Tenreiro, M. S. Hussein,

Effect of the breakup on the fusion and elastic scattering of weakly bound projectiles on ^{64}Zn. Phys. Rev. C. vol. 71, no. 3, p. 034608, Mar. 2005,https://doi.org/10.1103/PhysRevC.71.034608

[47] C. R. Morton, A. C. Berriman, M. Dasgupta, D. J. Hinde, J. O. Newton, K. Hagino, I. J. Thompson, Coupled-channels analysis of the ^{16}O+^{208}Pb fusion barrier distribution. Phys. Rev. C. vol. 60, no. 4, pp. 446081–4460811, Aug. 1999, https://doi.org/10.1103/PhysRevC.60.044608